International Journal of Modern Physics C
Vol. 21, No. 10 (2010) 1237–1254

DOI: 10.1142/S0129183110015804

World Scientific
www.worldscientific.com

SIMULATION OF NEWTONIAN AND NON-NEWTONIAN AXISYMMETRIC FLOW WITH AN AXISYMMETRIC LATTICE BOLTZMANN MODEL

X. F. LI, G. H. TANG*, T. Y. GAO and W. Q. TAO
State Key Lab of Multiphase Flow
School of Energy and Power Engineering
Xi'an Jiaotong University, Xi'an 710049, China
**ghtang@mail.xjtu.edu.cn*

Received 24 June 2010
Accepted 10 September 2010

Axisymmetric flow is of both fundamental interest and practical significance. A recently derived axisymmetric lattice Boltzmann model [J. G. Zhou, *Phys. Rev. E* **78**, 036701 (2008)] is adopted for studying several typical axisymmetric flows. First, the Hagen–Poiseuille flow in circular pipes is validated and the Poiseuille flow in annular cylinders is studied under different values of the radius ratio. Second, pulsatile flow in an axisymmetric pipe with a sinusoidal pressure gradient is conducted. Third, flows through pipes with various constrictions or expansions are discussed. Finally, we extend the axisymmetric lattice Boltzmann method for non-Newtonian flow. It is found that the obtained numerical results agree well with available analytical solutions. It is also observed that constriction or expansion in a pipe influences the velocity distribution of the flow significantly. In addition, the results demonstrate that the modified axisymmetric lattice Boltzmann model is capable of handling non-Newtonian flow.

Keywords: Lattice Boltzmann model; axisymmetric flow; constriction; expansion.

1. Introduction

The lattice Boltzmann method (LBM) has been successfully applied to different flow problems in science and engineering as an efficient and promising numerical method. Much attention has been devoted to axisymmetric flow due to its important practical applications. However, most previous studies on axisymmetric flows using the 3D LBM are based on the Cartesian coordinate system. In that way, the efficiency of simulation is low. Mathematically, if the azimuthal velocity equals zero, a 3D axisymmetric flow can be reduced to a quasi-2D problem in a cylindrical coordinate system. Therefore, developing an axisymmetric lattice Boltzmann model which depends on 2D Cartesian coordinates is highly desirable and feasible. Attention has been drawn to this field and the research on axisymmetric lattice Boltzmann models is growing.[1–11] Halliday *et al.*[1] first proposed an axisymmetric lattice Boltzmann model and successfully simulated steady flow in straight tubes.

They inserted two source terms dependent on the position and time into the microscopic evolution equation of the standard LBM and recovered the macroscopic equations with the Chapman–Enskog method. Lee *et al.*[3] proposed a revised model using the incompressible D2Q9 model instead of the standard D2Q9 model. Recently, four models have been proposed in succession. Reis and Phillips[4,5] derived their own model and validated the model through two benchmark problems. Zhou[5] found the above models have two main drawbacks: one is that the second source term is too complicated, and the other is that the added force is inconsistent with the lattice Boltzmann equation in dimensions. He developed an alternative axisymmetric lattice Boltzmann model and validated it with two flow problems. Chen *et al.*[7,8] proposed an axisymmetric model for isothermal flow and another one for thermal flow, respectively. Both models were derived from vorticity-stream-function equations while other existing models were based on "primitive-variables" Navier–Stokes equations. Most recently, Guo *et al.*[9] developed an axisymmetric lattice Boltzmann model from the continuous Boltzmann-BGK equation.

Comparing with some existing axisymmetric lattice Boltzmann models, we found that Zhou's model is fairly simple and efficient. Huang and Lu[10] recently showed that Zhou's model seems to be the simplest one and this model is most stable in terms of the sensitivity of relaxation time through theoretical and numerical analyses of three-type axisymmetric lattice Boltzmann models. In this regard, we adopt Zhou's model to investigate some typical axisymmetric flows and also extend this model to non-Newtonian flow.

The rest of the paper is organized as follows. Zhou's axisymmetric lattice Boltzmann model is briefly introduced in Sec. 2. In Sec. 3 some numerical simulations are carried out using the model. A brief conclusion is presented at the end.

2. Numerical Method

In our study, the Zhou's axisymmetric lattice Boltzmann method is employed. Now, we give a brief introduction to this model and details of the derivation can refer to Zhou's paper.[6] This model is derived from the standard D2Q9 model, and the nine lattice velocities of Zhou's model are given by

$$[\mathbf{e}_1, \mathbf{e}_2, \mathbf{e}_3, \mathbf{e}_4, \mathbf{e}_5, \mathbf{e}_6, \mathbf{e}_7, \mathbf{e}_8, \mathbf{e}_9] = \begin{bmatrix} 1 & 0 & -1 & 0 & 1 & -1 & -1 & 1 & 0 \\ 0 & 1 & 0 & -1 & 1 & 1 & -1 & -1 & 0 \end{bmatrix} c\,, \tag{1}$$

where $c = \Delta x/\Delta t$ is particle streaming speed (Δx, Δt are the lattice spacing and time step, respectively).

In this model, $f_\alpha(x, r, t)$ is the single particle density distribution function with velocity $\mathbf{e}_\alpha$ at position (x, r) and time t. The macroscopic variables such as mass density and momentum density can be obtained by summing over the distribution function $f_\alpha(x, r, t)$:

$$\rho = \sum_\alpha f_\alpha \quad \text{and} \quad \rho\mathbf{u} = \sum_\alpha f_\alpha \mathbf{e}_\alpha\,. \tag{2}$$

The equilibrium distribution function is defined as

$$f_\alpha^{\mathrm{eq}} = \omega_\alpha \rho \left[1 + \frac{3}{c^2}(\mathbf{e}_\alpha \cdot \mathbf{u}) + \frac{9}{2c^4}(\mathbf{e}_\alpha \cdot \mathbf{u})^2 - \frac{3}{2c^2}\mathbf{u}^2\right], \quad \alpha = 1, 2, 3, \ldots, 9, \tag{3}$$

where $\omega_\alpha = 1/9$ for $\alpha = 1$, 2, 3, 4, $\omega_\alpha = 1/36$ for $\alpha = 5$, 6, 7, 8, and $\omega_9 = 4/9$.

The axisymmetric lattice Boltzmann model includes two main steps: the collision and propagation steps. In the collision step, the following formula is implemented:

$$f_\alpha^+(x, r, t) = f_\alpha(x, r, t) - \frac{1}{\tau}(f_\alpha - f_\alpha^{\mathrm{eq}}) + \theta \Delta t + \frac{\Delta t}{\gamma c^2}(e_{\alpha x} F_x + e_{\alpha r} F_r), \tag{4}$$

where f_α^+ is the post-collision density distribution function of particles, τ is the single relaxation time, θ is a source term which is calculated through Eq. (5), F_x and F_r are force terms in x and r directions, respectively. They are given by Eqs. (6) and (7). $e_{\alpha x}$ or $e_{\alpha r}$ is the particle's velocity in x or r link. γ is a constant, here $\gamma = 6$.

$$\theta = -\frac{\rho}{9}\frac{u_r}{r}, \tag{5}$$

$$F_x = -\frac{\rho u_x u_r}{r} + \frac{\rho \upsilon}{r}\frac{\partial u_x}{\partial r}, \tag{6}$$

$$F_r = -\frac{\rho u_r u_r}{r} + \frac{\rho \upsilon}{r}\frac{\partial u_r}{\partial r} - \frac{\rho \upsilon u_r}{r^2}. \tag{7}$$

In the above equations, u_x and u_r are the velocity in x and r directions, respectively. The fluid kinematic viscosity υ is defined in Eq. (8). In addition, we note that along the axis of symmetry, singular source terms of type $1/r$ exist in Eqs. (5)–(7). In order to avoid the singularity at $r = 0$, we arrange that the centerline of the pipe is in the middle of the two consecutive horizontal lattice lines as Ref. 5 mentioned.

$$\upsilon = c_s^2 \Delta t(\tau - 0.5), \tag{8}$$

where c_s is the speed of sound in the fluid and $c_s = c/\sqrt{3}$.

In the propagation step, the new distribution function obtained from the collision process will propagate to neighbor cells. In this process, the following formula is implemented:

$$f_\alpha(\mathbf{x} + \mathbf{e}_\alpha \Delta t, t + \Delta t) = f_\alpha^+(\mathbf{x}, t). \tag{9}$$

We know that the shear stress tensor is of great importance in some flow studies. For this axisymmetric lattice Boltzmann method, the shear stress τ_{rx} can be computed from Eq. (10),

$$\tau_{rx} = \rho \upsilon \left[\frac{\partial u_x}{\partial r} + \frac{\partial u_r}{\partial x}\right] = -\left(1 - \frac{1}{2\tau}\right) \sum_\alpha e_{\alpha x} e_{\alpha r}(f_\alpha - f_\alpha^{\mathrm{eq}}) + O(\varepsilon^2). \tag{10}$$

Note that Eq. (10) is usually computed with second-order accuracy during the collision process in the axisymmetric LBM evolution. Therefore, the stress tensor

can be obtained independent of the velocity field, in contrast to most traditional CFD methods which estimate the stress tensor from the obtained velocity field. This saves computational resource without a need to get the derivatives of velocity profiles.

In the velocity derivations above in Eqs. (6)–(7), terms of $\partial_r u_x$ and $\partial_r u_r$ can be easily obtained through the following Eqs. (11) and (12), respectively:

$$\frac{\partial u_x}{\partial r} = -\frac{3}{\rho\tau c^2 \Delta t} \sum_{\alpha} e_{\alpha x} e_{\alpha r} (f_\alpha - f_\alpha^{\mathrm{eq}}) - \frac{\partial u_r}{\partial x}\,, \tag{11}$$

$$\frac{\partial u_r}{\partial r} = -\frac{3}{2\rho\tau c^2 \Delta t} \sum_{\alpha} e_{\alpha r} e_{\alpha r} (f_\alpha - f_\alpha^{\mathrm{eq}}) - \frac{1}{2}\frac{u_r}{r}\,. \tag{12}$$

Note that here we calculated the term $\partial u_r/\partial x$ in Eq. (11) still with the finite difference method.

3. Numerical Simulation

3.1. *Hagen–Poiseuille flow*

We first simulate the Hagen–Poiseuille flow to validate Zhou's axisymmetric lattice Boltzmann model. The Hagen–Poiseuille flow is an axisymmetric steady, laminar flow of a viscous fluid through a pipe driven by a constant external force. The analytical dimensionless velocity of the Hagen–Poiseuille flow driven by a constant pressure gradient through a pipe with radius R is Ref. 5

$$\frac{u(r)}{u_m} = 2\left[1 - \left(\frac{r}{R}\right)^2\right]. \tag{13}$$

The viscosity shear stress in a rigid circular tube is

$$\tau_{rx} = -\frac{1}{2}\frac{dp}{dx} r\,. \tag{14}$$

In this case, the nonslip boundary conditions at the upper and lower walls proposed by Zou and He[12] were adopted. For the inlet and outlet boundary conditions, the periodic boundary conditions were applied. Moreover, the constant pressure gradient as a body force is added to the existing force term F_x,

$$F_x = -\frac{\rho u_x u_r}{r} + \frac{\rho\upsilon}{r}\frac{\partial u_x}{\partial r} + \frac{dp}{dx}\,. \tag{15}$$

In the simulation, $dp/dx = 5 \times 10^{-5}$, $\tau = 1.05$ and 20×80 lattices are used. Figure 1 presents the variation of dimensionless axial velocity with position r/R. We can see that the numerical results agree well with the analytical solutions, demonstrating the model's capability of handling steady axisymmetric flow. Figure 2 shows the dimensionless shear stress distribution along the radius, in which the computational result is also in good agreement with the analytical solution.

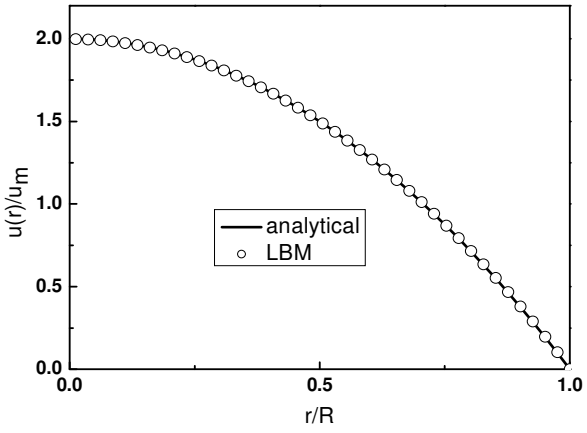

Fig. 1. Velocity comparison of Hagen–Poiseuille flow.

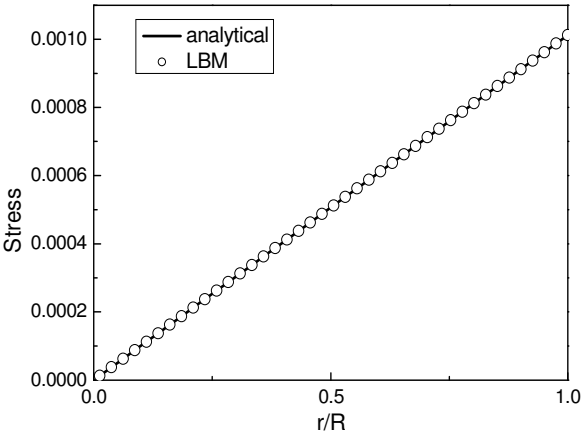

Fig. 2. Dimensionless shear stress comparison of Hagen–Poiseuille flow.

3.2. *Flow through a concentric annulus*

We then consider steady axial laminar flow in the annular space between two concentric cylinders driven by a constant pressure gradient schematic in Fig. 3. There are no slip at the inner wall ($r = R_1$) and outer wall ($r = R_2$). We define the radius ratio of outer cylinder to inner cylinder as k. Obviously, as $k \to \infty$, the flow recovers to the Hagen–Poiseuille flow which has been shown in Sec. 3.1. The treatment of the boundary conditions is the same as that in the Hagen–Poiseuille flow.

The analytical solution for the velocity profile is Ref. 13

$$u(r) = \frac{1}{4\upsilon\rho}\frac{dp}{dx}\left[r^2 - R_2^2 - \frac{R_2^2 - R_1^2}{\ln(R_2/R_1)}\ln\frac{r}{R_2}\right], \tag{16}$$

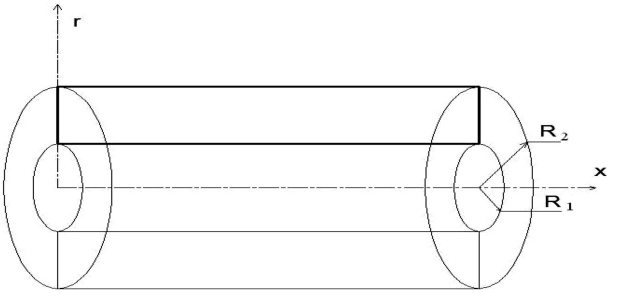

Fig. 3. Schematic of the geometry of flow through a concentric annulus.

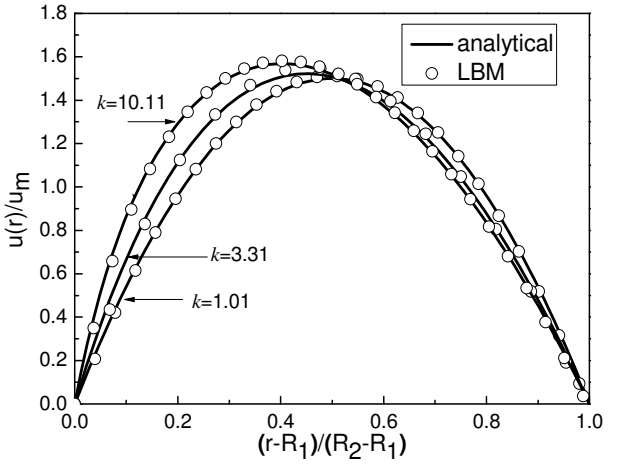

Fig. 4. Velocity profile for flow through concentric annulus with radius ratio $k = 10.11$, 3.31, and 1.01.

and the average velocity is

$$u_m = -\frac{1}{8\upsilon\rho}\frac{dp}{dx}\left[R_2^2 + R_1^2 - \frac{R_2^2 - R_1^2}{\ln(R_2/R_1)}\right] . \tag{17}$$

Figure 4 shows the normalized velocity profiles as u/u_m for flow through concentric annulus with $k = 1.01$, 3.31, and 10.11. The numerical results agree well with the analytical solutions. The figure also shows that the velocity profile leans toward the inner cylinder as the radius ratio k increases, which is consistent with Ref. 14.

3.3. *Pulsatile flow in a circular pipe*

Pulsatile flow in a circular pipe (3D Womersley flow) is also a typical axisymmetric flow and has important applications. It is driven by a periodic pressure gradient at

the inlet of the pipe and the pressure gradient is usually given by

$$\frac{\partial p}{\partial x} = -P^* e^{iwt}\,, \tag{18}$$

where P^* is the maximum amplitude of the sinusoidally varying pressure gradient and $\omega = 2\pi/T$ is the angular frequency, in which T is the period.

The characteristic velocity u_c is defined as

$$u_c = \frac{P^*\alpha^2}{4\omega\rho} = \frac{P^*R^2}{4\rho\upsilon}\,, \tag{19}$$

which is the velocity that would be observed at the center of the pipe if a constant forcing term P^* is applied in the limit of $\alpha \to 0$ (steady flow), where $\alpha = R\sqrt{\omega/\upsilon}$ is the Womersley number.

The analytical solution for the axial velocity in axisymmetric pipe pulsatile flow is[15]

$$u(r,t) = \mathrm{Re}\left\{\frac{P^*}{i\omega\rho}\left[1 - \frac{J_0[(1/\sqrt{2})(-\alpha + i\alpha)(r/R)]}{J_0[(1/\sqrt{2})(-\alpha + i\alpha)]}\right] e^{i\omega t}\right\}\,, \tag{20}$$

where J_0 is the zeroth-order Bessel function of the first type, i is the imaginary unit and Re denotes the real part of a complex number.

In this study, boundary treatments for upper/lower wall and inlet/outlet are the same as the two cases mentioned above. For the Womersley flow, the periodic pressure gradient is applied as a periodic body force. The body force is added to the existing force F_x

$$F_x = -\frac{\rho u_x u_r}{r} + \frac{\rho\upsilon}{r}\frac{\partial u_x}{\partial r} + P^* e^{i\omega t}\,, \tag{21}$$

where P^* is the maximum amplitude of the sinusoidally varying pressure gradient.

In the simulation, $\rho = 1$, $P^* = 0.0001$, $R = 30$, $T = 1000$, $\alpha = 9.36$, $u_c = 0.348$, $\mathrm{Re} = 319$, $\tau = 0.7$, and 10×60 lattices are used. The simulation begins with an initial condition of zero velocity. The numerical solutions at different times are obtained after an initial run of $10T$ steps.

The velocities along the diameter of pipe are normalized by u_c. The numerical and analytical dimensionless velocities are compared as indicated in Figs. 5 and 6, showing good agreement. Figure 5 shows the comparison between numerical results and analytical solutions when the velocity is increasing at different time $t = nT/16$ ($n = 0, 1, 2, 3, 12, 13, 14, 15$). Figure 6 shows comparison between numerical results and analytical solutions when the velocity is decreasing at different time $t = nT/16$ ($n = 4, 5, 6, 7, 8, 9, 10, 11$).

Figure 7 shows the dimensionless velocity profile over half a period for $\alpha = 1.149$. In this case, we set $\mathrm{Re} = 1.7$, $\tau = 2$, $T = 4000$ and the axial grid number $N_r = 40$, which is a viscous-dominated system.[16] Figure 8 presents the normalized velocity profile over half a period for $\alpha = 17.33$. In this case, we set $\mathrm{Re} = 1449$, $\tau = 0.7$, $T = 800$ and $N_r = 100$, which is a momentum-dominated system.[16]

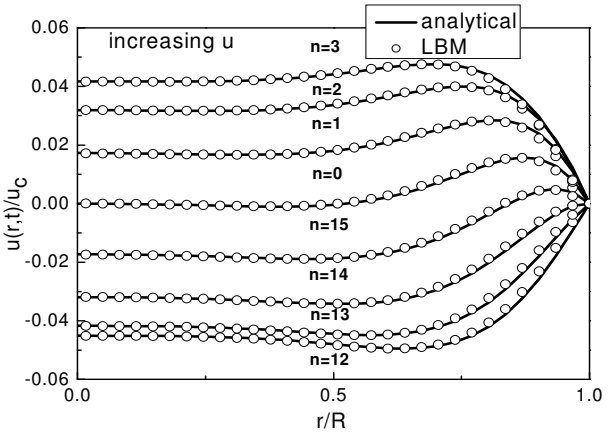

Fig. 5. Profiles of increasing dimensionless velocity along the radius at different times.

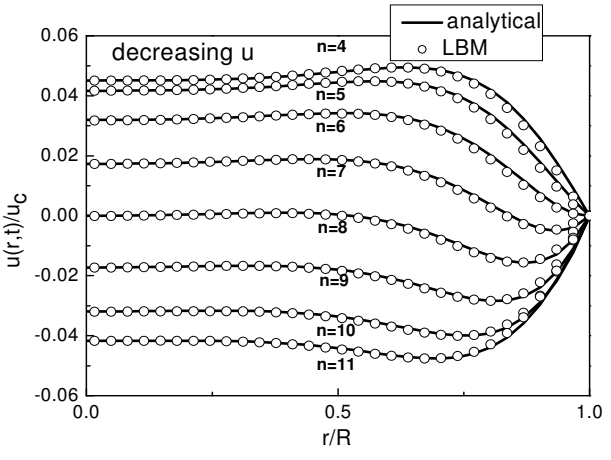

Fig. 6. Profiles of decreasing dimensionless velocity along the radius at different times.

To investigate the effect of pressure gradient in Womersley flow, we introduce a velocity error formula which is illustrated in Ref. 16. The error is defined at each time step as follows,

$$\xi = \frac{\sum_i |u(r_i) - u_a(r_i)|}{\sum_i |u_a(r_i)|}\,, \tag{22}$$

where $u(r_i)$ is the numerical velocity, and $u_a(r_i)$ is the analytical solution at r_i. The overall average error $\langle\xi\rangle$ is averaged over the period.

In Table 1, we can see that the variety of pressure gradient has little effect on pulsatile flow by using Zhou's axisymmetric lattice Boltzmann model while in Ref. 16 the overall average error varies obviously with different pressure gradients.

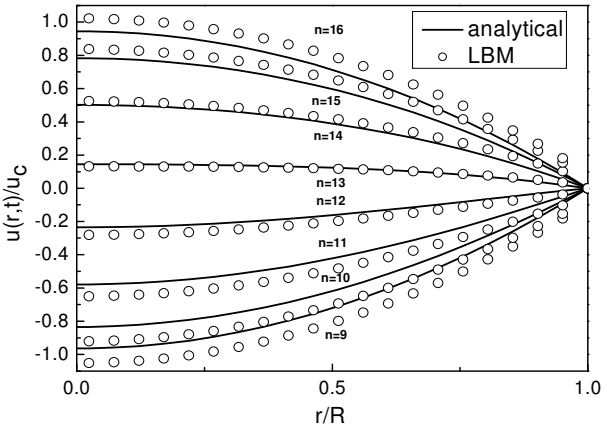

Fig. 7. Velocity profiles along the radius over half a period when $\alpha = 1.149$.

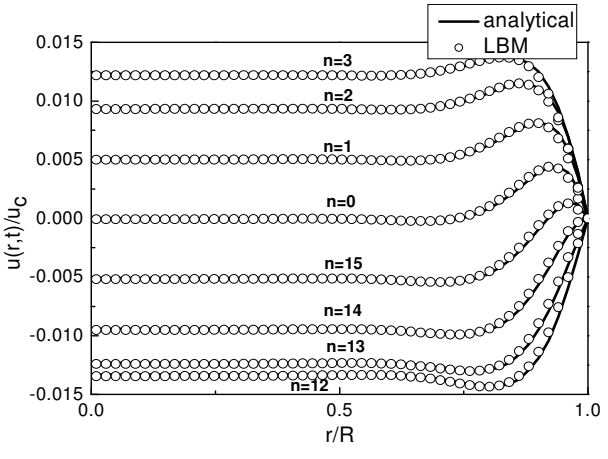

Fig. 8. Velocity profiles along the radius over half a period when $\alpha = 17.33$.

3.4. *Steady flow through constricted pipes*

The flow in constricted pipes has been of great interest to biodynamicists. Although the actual geometry of a stenotic artery may be complex and varied, it is frequently simplified as a symmetric constriction in a cylindrical tube.[17] Several researchers have studied steady flow through an axisymmetric tube with constriction. Smith[18] studied steady flow through an axisymmetric stenosis using an analytical method. Huang *et al.*[19] investigated steady flow through tubes with constrictions using LBM with D3Q19 model. We study the flow using Zhou's axisymmetric lattice Boltzmann method due to its simple and efficient feature.

In this case, the geometry of the constriction is described by a cosine function curve. The geometry of the constricted pipe is shown in Fig. 9 and the radius of

Table 1. The overall average error $\langle\xi\rangle$ for different pressure gradients.

Cases	Re	P^*	Error $\langle\xi\rangle$
1	31.9	0.00001	1.41E-2
2	319	0.0001	1.41E-2
3	1596	0.0005	1.40E-2

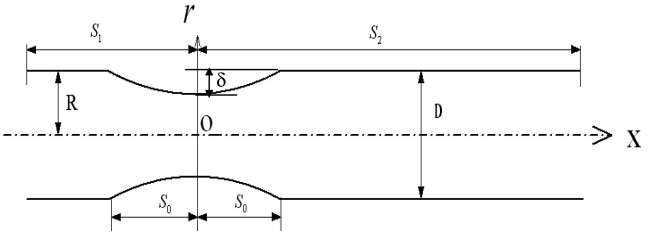

Fig. 9. Schematic of the geometry of a constricted pipe.

the stenosis $r(x)$ is described by the following function

$$r(x) = R - \frac{\delta}{2}\left(1 + \cos\frac{\pi x}{S_0}\right), \quad (-S_0 < x < S_0), \tag{23}$$

where R is the radius of the nonstenotic part of the pipe, δ is the radial height of the stenosis, the axial length of the stenosis is $2S_0$, and $S_0 = D$. In this study, we compute three cases of stenosis radial height, $\delta = R/4$, $R/3$, and $R/2$. As schematic in Fig. 9, we set $S_1 = 3D$ and $S_2 = 8D$ to make sure that the flow is fully developed at the outlet.

In our simulation, a fully developed parabolic velocity profile is imposed at the inlet boundary and the zero pressure gradient is used at the outlet boundary. The center value of the inlet parabolic velocity keeps at $u_c = 0.01$. The employed lattice number is 880×80 and the Reynolds number $\mathrm{Re} = 4.1$ ($\mathrm{Re} = u_c D/\upsilon$). We deal with the wall boundary conditions using the bounce-back scheme. The inlet velocity boundary is applied with Zou and He velocity boundary treatment and the outlet pressure is specified from the next inner nodes.[12] The normalized axial and radial velocity profiles at $x = 0$ are shown in Figs. 10 and 11, respectively for three values of the stenosis radial height δ. We can see that the axial velocity increases and exhibits sharper as the stenosis radial height increases. In Fig. 11, the obvious reverse flow is observed and the absolute radial velocity also increases as the stenosis radial height increases. The results show that the stenosis radial height has significant effect on the velocity and thus the wall shear stress distribution.

3.5. *Steady flow through expanded pipes*

We also study steady flow through pipes with local expansion of cosine function shape. The geometry of the expansion is shown in Fig. 12. Radius of the expansion

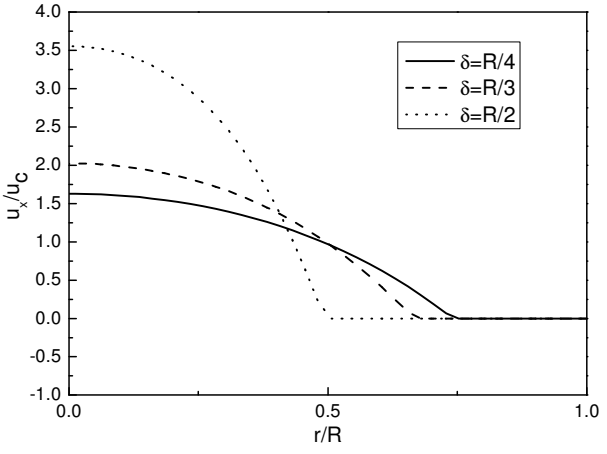

Fig. 10. Axial velocity profiles in constricted pipe for three different constriction radial heights.

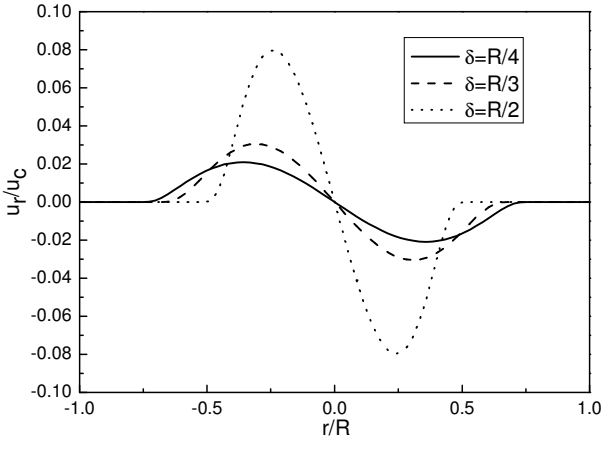

Fig. 11. Radial velocity profiles in constricted pipe for three different constriction radial heights.

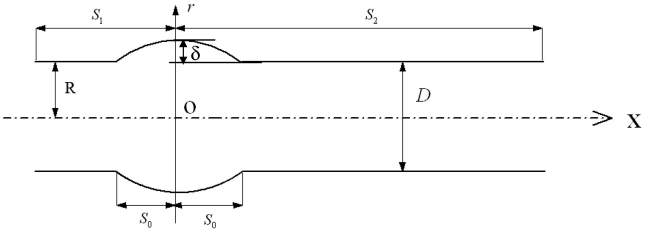

Fig. 12. Schematic of the geometry of an expanded pipe.

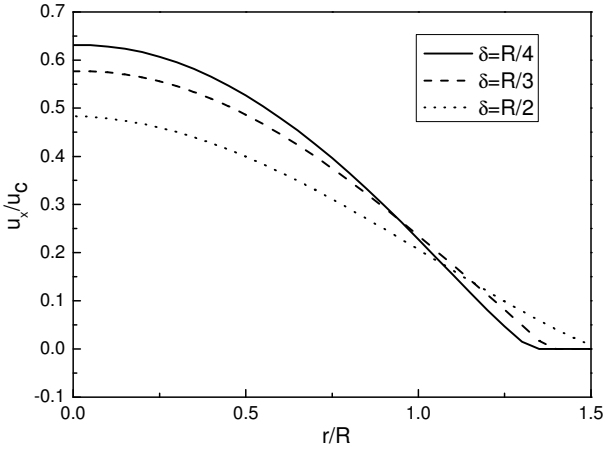

Fig. 13. Axial velocity profiles in expanded pipe for three different expansion radial heights.

$r(x)$ is described by the following function

$$r(x) = R + \frac{\delta}{2}\left(1 + \cos\frac{\pi x}{S_0}\right), \quad (-S_0 < x < S_0), \tag{24}$$

where R is the radius of the nonexpanded part of the pipe, δ is the radial height of the expansion, the axial length of the expansion is $2S_0$ with $S_0 = D$. In this study, we also compute three cases of expansion height, $\delta = R/4$, $R/3$, and $R/2$. As schematic in Fig. 12, we have $S_1 = 3D$ and $S_2 = 8D$ to make sure the flow fully developed at the outlet.

In our simulation, a fully developed parabolic velocity profile is also imposed at the inlet boundary and the zero pressure gradient is used at the outlet boundary. The center value of the inlet parabolic velocity is $u_c = 0.01$ and the Reynolds number Re = 4.1 (Re $= u_c D/\upsilon$). The boundary conditions are treated with the same method as the flow through a constricted pipe. We can see that the axial velocity profile at $x = 0$ shown in Fig. 13 decreases as the expansion height δ increases, while the radial velocity at $x = 0$ shown in Fig. 14 increases as the expansion height increases. This validates that the expansion in a pipe significantly influences the velocity of the flow, hence leading to a great effect on the wall stress tensor in the flow. For human carotid with local expansion, these changes of velocity and thus the wall shear stress caused by expansion will influence the structure and the function of the vessel significantly.

3.6. *Non-Newtonian flow in cylindrical channels*

The existing axisymmetric flows studied are all limited to Newtonian fluid. The flow behavior of non-Newtonian fluid is of high interest in various areas of science and technology. Especially, due to the convenient implementation for the complex geometries, the LBM is of great potential on the simulation of non-Newtonian flow

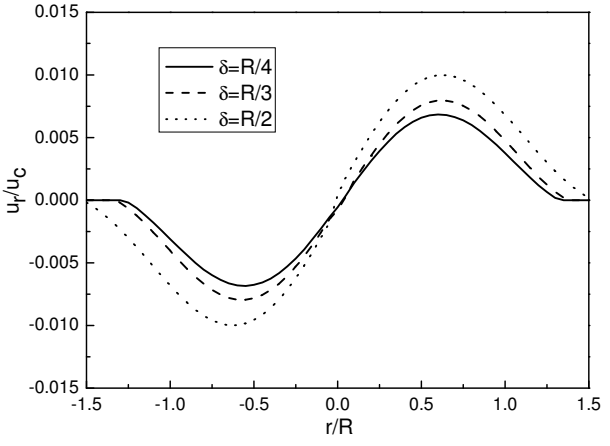

Fig. 14. Radial velocity profiles in expanded pipe for three different expansion radial heights.

behaviors in porous media as investigated by Morais *et al.*[20] Therefore, we investigate non-Newtonian flow in cylindrical channels using the present axisymmetric lattice Boltzmann model. In the commonly used power-law model for non-Newtonian fluid, the viscosity is given by

$$\eta = \eta_0 \dot{\gamma}^{n-1}\,, \tag{25}$$

where the shear rate-related $\dot{\gamma}$ is $\dot{\gamma} = |du/dr|$ and the parameter n is the power-law exponent which determines the response of the fluid to change in shear rate. The fluid is shear thinning for $n < 1$, shear thickening for $n > 1$ and Newtonian fluid with shear-independent viscosity η_0 for $n = 1$.

Coupling Eqs. (8), (11) and (25), together with $\eta = \rho\upsilon$, we have a shear-dependent relaxation time τ at each node in the lattice Boltzmann evolution Eq. (4). Note that the term $\partial u/\partial r$ can be computed with Eq. (11). The quantity $e_{\alpha x}e_{\alpha r}(f_\alpha - f_\alpha^{\rm eq})$ in Eq. (11) is usually computed with second-order accuracy during the collision process in the axisymmetric LBM evolution. This benefit without a need to get the derivatives of velocity profiles in computing the stress tensor and non-Newtonian viscosity is clear when dealing with flow in complex geometry or flows characterized by large velocity gradients.

A pressure-driven non-Newtonian fluid flow in circular pipe is considered first. In the simulation, $dp/dx = 5 \times 10^{-5}$ is applied along the streamwise direction as the external force. For the power-law fluid, an analytical solution for streamwise velocity across the tube is given by Ref. 21

$$\frac{u}{u_m} = \frac{3n+1}{n+1}\left[1 - \left(\frac{r}{R}\right)^{n+1/n}\right]\,, \tag{26}$$

where u_m is the mean velocity across the tube.

Simulation were ran for $n = 0.7$, $n = 1$, $n = 1.5$, and $n = 2$ to test the axisymmetric LBM accuracy for a range of non-Newtonian behaviors. Figure 15

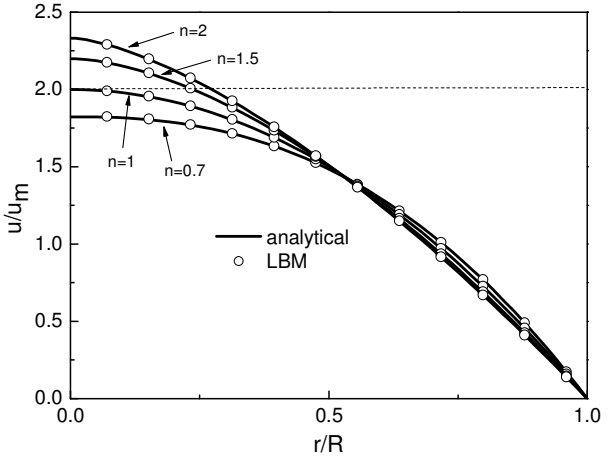

Fig. 15. Velocity comparison of non-Newtonian flow in circular pipe.

shows the axisymmetric LBM results (symbols) compared to normalized analytical velocity profiles (solid lines) over the range of n parameter values. The agreement with the analytical solutions is quite good. Comparing shear thinning flow ($n = 0.7$) with Newtonian flow ($n = 1$), we can see a general flattening of the velocity profile. In contrast, the velocity profiles for $n = 1.5$ and $n = 2$ show greater curvature around the center peak velocity. The ratio of the center peak velocity to the mean velocity increases as the index n increases.

The present model is also extended to non-Newtonian flow in annular pipe. The radius ratio of outer cylinder to inner cylinder is also defined as $k = R_2/R_1$. The treatment of the boundary conditions is the same as the non-Newtonian fluid flow in circular pipe.

Figures 16(a)–16(c) show the normalized velocity profiles as u/u_m for flow through concentric annulus with $k = 1.01$, 2, and 10. As shown in Fig. 16, for $n = 0.8$ we can see a general flattening of the velocity profile. Conversely, the velocity profiles for $n = 1.5$ and $n = 1.8$ show great curvature near the center peak velocity. The larger the power-law exponent value n, the greater the curvature. In addition, we can see that the velocity profile leans from the inner surface to the annulus center as the power-law exponent increases, especially in the case of large radius ratio shown in Fig. 16(c). As the radius ratio k increases from Figs. 16(a) to 16(c), the velocity profile leans toward the inner cylinder.

In addition, we also studied the non-Newtonian flow in constricted pipes and expanded pipes, which have important applications in hemodynamics. The normalized axial velocity profiles at $x = 0$ and $x = D$ in constricted pipes and expanded pipes are shown in Figs. 17 and 18, respectively. We can see that the power-law exponent value n causes different velocity distributions in the constricted region. The increased velocity of shear thickening fluid with $n > 1$ over shear thinning

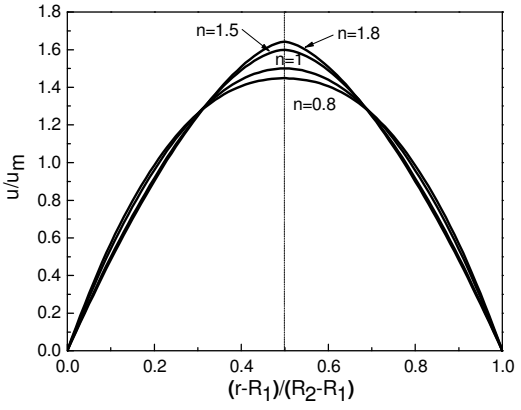

(a)

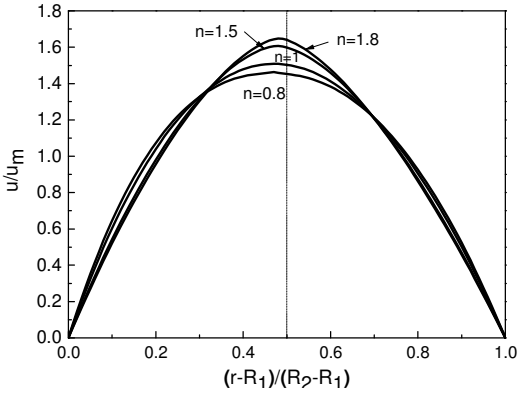

(b)

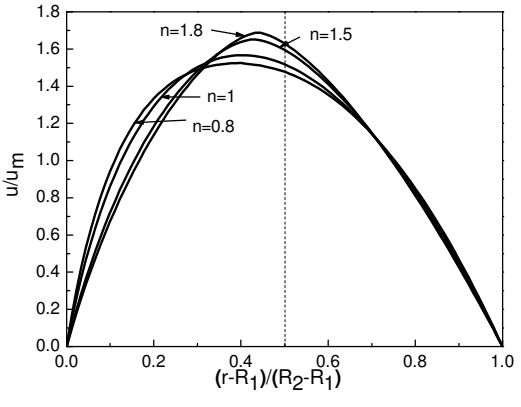

(c)

Fig. 16. Velocity profiles for non-Newtonian flow in annular pipe. (a) $k = 1.01$, (b) $k = 2$, and (c) $k = 10$.

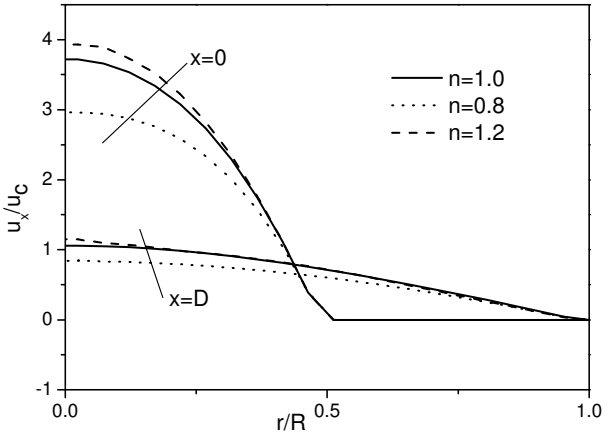

Fig. 17. Non-Newtonian effect on axial velocity profiles in a constricted pipe.

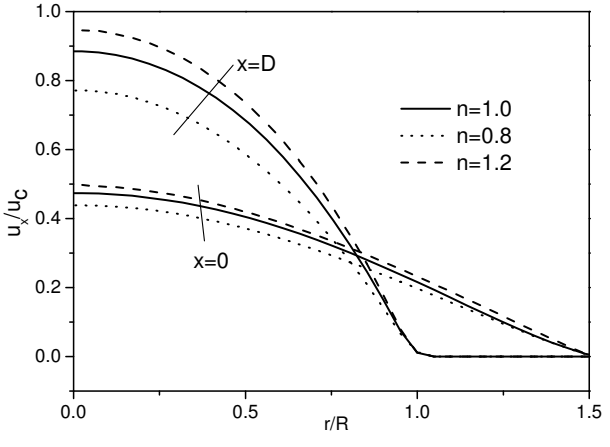

Fig. 18. Non-Newtonian effect on axial velocity profiles in an expanded pipe.

fluid is more obvious at the peak of the constriction than at other locations. On the contrary, the increased velocity of shear thickening fluid with $n > 1$ over shear thinning fluid is less obvious at the peak of the expansion than at other locations.

4. Conclusions

In this study, we have adopted an axisymmetric lattice Boltzmann method to study several typical axisymmetric flows and have extended it to non-Newtonian flow. Firstly, we validated the present model by simulating Hagen–Poiseuille flow and flow through a concentric annulus. Numerical results both agree well with the analytical solutions. We also found that the velocity profile for flow through a concentric annulus leans towards the inner cylinder as the radius ratio of k increases. Secondly,

we applied the model to pulsatile flow in a circular pipe and found that the numerical results obtained by the present model are also in good agreement with the analytical solutions. The results show that the Womersley number has significant effect on the pattern of the flow, while the amplitude of pressure gradient has little effect on the flow. Then, flow through pipes with constriction and expansion was discussed respectively. We found that the constrictions or the expansions in a pipe influence the velocity of the flow significantly, which will lead to a great influence on the wall shear stress.[22] Lastly, we extend the axisymmetric LBM to non-Newtonian flow in cylindrical channels, and the results show that the power-law exponent n plays an important role on power-law fluid flow. In addition, for power-law fluid flow in annulus, the velocity profile leans from the inner surface toward the annulus center as the power-law exponent n increases. Regarding non-Newtonian flow in non-straight pipes, the non-Newtonian property behaves more significantly at the peak of the constriction in constricted pipe while in expanded pipe, it behaves less importantly at the peak of the expansion than at other locations.

Acknowledgments

This work was supported by the National Natural Science Foundation of China (Grant Nos. 50776067 and 50806059) and the Program for NCET in University (Grant No. NCET-07-0676).

References

1. I. Halliday, L. A. Hammond, C. M. Care, K. Good and A. Stevens, *Phys. Rev. E* **64**, 011208 (2001).
2. X. D. Niu, C. Shu and Y. T. Chew, *Int. J. Mod. Phys. C* **14**, 785 (2003).
3. T. S. Lee, H. Huang and C. Shu, *Int. J. Mod. Phys. C* **17**, 645 (2006).
4. T. Reis and T. N. Phillips, *Phys. Rev. E* **75**, 056703 (2007).
5. T. Reis and T. N. Phillips, *Phys. Rev. E* **77**, 026703 (2008).
6. J. G. Zhou, *Phys. Rev. E* **78**, 036701 (2008).
7. S. Chen, J. Tölke, S. Geller and M. Krafczyk, *Phys. Rev. E* **78**, 046703 (2008).
8. S. Chen, J. Tölke, S. Geller and M. Krafczyk, *Phys. Rev. E* **79**, 016704 (2009).
9. Z. Guo, H. Han, B. Shi and C. Zheng, *Phys. Rev. E* **79**, 046708 (2009).
10. H. Huang and X. Y. Lu, *Phys. Rev. E* **80**, 016701 (2009).
11. H. Huang and X. Y. Lu, *Int. J. Mod. Phys. C* **20**, 1145 (2009).
12. Q. Zou and X. He, *Phys. Fluids* **9**, 1591 (1997).
13. F. M. White, *Fluid Mechanics* (McGraw-Hill, New York, 2002).
14. J. E. Mott and D. D. Joseph, *Phys. Fluids* **11**, 2065 (1968).
15. A. M. Artoli, A. G. Hoekstra and P. M. A. Sloot, *Int. J. Mod. Phys. C* **13**, 1119 (2002).
16. T. S. Lee, H. B. Huang and C. Shu, *Int. J. Numer. Meth. Fluids* **49**, 99 (2005).
17. Q. Long, X. Y. Xu, K. V. Ramnarine and P. Hoskins, *J. Biomech.* **34**, 1229 (2001).
18. F. T. Smith, *J. Fluid Mech.* **90**, 725 (1979).
19. H. B. Huang, T. S. Lee and C. Shu, *Int. J. Numer. Meth. Heat Fluid Flow* **16**, 185 (2006).

20. A. F. Morais, H. Seybold, H. J. Herrmann and J. S. Andrade, *Phys. Rev. Lett.* **103**, 194502 (2009).
21. L. C. Zheng, X. X. Zhang and L. X. Ma, *Chin. Phys. Lett.* **25**, 195 (2008).
22. A. M. Artoli, A. G. Hoekstra and P. M. A. Sloot, *Comput. Fluids* **35**, 227 (2006).